J Mater Sci (2017) 52:11453–11466

Composites

Synthesis and characterization of direct Z-scheme $Bi_2MoO_6/ZnIn_2S_4$ composite photocatalyst with enhanced photocatalytic oxidation of NO under visible light

Shipeng Wan[1,2], Qin Zhong[1,2,*], Man Ou[1,2], and Shule Zhang[1,2]

[1] School of Chemical Engineering, Nanjing University of Science and Technology, Nanjing 210094, Jiangsu, People's Republic of China

[2] Nanjing AIREP Environmental Protection Technology Co., Ltd., Nanjing 210091, Jiangsu, People's Republic of China

Received: 3 March 2017
Accepted: 9 June 2017
Published online: 23 June 2017

ABSTRACT

In the work, the direct Z-scheme $Bi_2MoO_6/ZnIn_2S_4$ (BMO + x%–ZIS; x = 2, 4, 6, 8, 10) composite semiconductor photocatalysts were successfully constructed by using a simple wet impregnation method. Then the oxidation of NO (~400 ppm) with H_2O_2 solution injected (0.0075 mL min^{-1}) was used to estimate their photocatalytic performances under visible light. The results indicate that BMO + x%–ZIS composites exhibit enhanced photocatalytic activity, wherein the BMO + 6%–ZIS composite possesses the highest photocatalytic activity (84.94%). The enhanced photocatalytic performance is ascribed to the low rate of recombination of photogenerated electrons and holes and the production and participation of active radical species as confirmed by PL spectra and trapping experiment as well as fluorescence spectra. The existence of H_2O_2 is also essential in the improvement of the photocatalytic efficiency via production of more active species. The photocatalytic product in the PCO of NO is NO_3^-, which was detected by ion chromatography. In addition, the mechanism of PCO of NO was discussed detailedly. The results indicate that ·OH plays an important role, but the effect of $\cdot O_2^-$ is also crucial in the experiment of PCO of NO system.

Introduction

Semiconductor photocatalysis is a potential green chemical technique, employing solar light as energy source for water splitting, organic pollution degradation and NO oxidation [1–5]. Since the discovery of Honda–Fujishima effect in 1972 [6], an immense amount of visible-light-responsive semiconductor photocatalysts have been developed, including Bi-based, Ag-based, Co-containing and Cu-containing photocatalysts [7–10]. Among them, Bi-based semiconductor photocatalysts have attracted worldwide

Address correspondence to E-mail: zq304@njust.edu.cn

DOI 10.1007/s10853-017-1283-3

attention due to the low cost of synthetic materials and widespread availability. Up to now, the Bi-containing semiconductor photocatalysts mainly include Bi_2MoO_6, $BiVO_4$, $Bi_2O_2CO_3$, Bi_2WO_6, BiOCl(Br), Bi_2O_3, Bi_2S_3, and so forth [11–17]. Bi_2MoO_6, a typical Aurivillius-related oxide, possesses a suitable band gap, capable of capturing visible light and excellent photocatalytic activity for organic pollution degradation and water splitting [11, 18]. However, the practical application of Bi_2MoO_6 is still limited due to the poor quantum yield, which is caused by the rapid recombination of photoinduced charges and holes. To prolong the lifetimes of photoinduced charge carriers and improve the visible-light-driven photocatalytic performance of Bi_2MoO_6, different modifications have been attempted. Therein large amounts of Bi_2MoO_6-based composite photocatalysts (e.g., $Bi_2O_2CO_3/Bi_2MoO_6$ [19], TiO_2–$Bi_2MoO_6/Bi_{3.64}Mo_{0.36}O_{6.55}$ [20], Bi_2MoO_6/carbon nanofibers [21]) have been synthesized in attempt to enhance the separation of photoinduced charges and holes.

As alternatives, the ternary metal sulfides (e.g., $ZnIn_2S_4$, CdIn2S4, $CuGaS_2$, $CaIn_2S_4$, $CuInS_2$) have received worldwide attention due to their unique optoelectronic properties, chemical stability and outstanding photocatalytic activity [22–24]. In particular, the $ZnIn_2S_4$ (ZIS) not only possesses appropriate band gap and enhanced photocatalytic activity, but also can be easily synthesized under relative mild conditions using different precursors [25, 26]. Now it has been applied in water splitting, organic pollution degradation and photocatalytic CO_2 reduction [27–30], etc. However, the ternary metal sulfides have the defect of self-photocorrosion. What's more, it is still a difficult problem to transfer the photoinduced electron–hole pairs and enhance their separation rate for an isolated ternary metal sulfide component. Obviously, it is desirable to explore novel process route to enhance the transfer efficiency of photoinduced electrons and holes for ternary metal sulfides.

To the best of our knowledge, little attention has been given to PCO of NO in flue gas of power plant over $Bi_2MoO_6/ZnIn_2S_4$ (BMO + x%–ZIS; x = 2, 4, 6, 8, 10) composite photocatalysts. Herein, we have designed direct Z-scheme BMO + x%–ZIS composite photocatalysts by a facial wet impregnation method, which were expected to improve the separation rate of photoinduced electrons and holes in ZIS and BMO effectively, thus improving the photocatalytic performance. The enhanced PCO efficiency of NO for the BMO + x%–ZIS composite photocatalysts was achieved under visible light, and the reasons contributing to this were analyzed minutely. Additionally, the photocatalytic reaction production and possible mechanism of PCO of NO were also investigated in this study.

Experimental section

Preparation of $Bi_2MoO_6/ZnIn_2S_4$ composites

All chemicals purchased were used directly. Bi_2MoO_6 was prepared by solvothermal method. In a typical synthetic method, 3.4 mmol $Bi(NO_3)_3{\cdot}5H_2O$ and 1.7 mmol $Na_2MoO_4{\cdot}2H_2O$ were, respectively, dissolved in 10 mL of ethylene glycol (EG) under ultrasonic conditions, labeled A solution and B solution, respectively. Then the B solution was added dropwise into B solution to form a homogeneous mixture solution under stirring conditions. After that, 40 mL ethanol was slowly added dropwise into the above solution, followed by stirring for 30 min. The resulting buff solution was transferred into a 100 mL Teflon-lined stainless steel autoclave, maintaining t 180 °C for 12 h. Subsequently, the autoclave was cooled to room temperature naturally. The obtained samples were centrifuged and washed with water and ethanol and dried at 80 °C overnight in a vacuum oven. In the course of time, the as-prepared sample was annealed at 400 °C for 3 h and labeled as BMO.

$ZnIn_2S_4$ was synthesized by the hydrothermal method. Briefly, 5 mmol $Zn(NO_3)_2{\cdot}4H_2O$, 10 mmol $In(NO_3)_3{\cdot}xH_2O$ (molecular weight 301 g mol^{-1}) and 40 mmol thioacetamide were dissolved in 80 mL deionized water in succession and stirred for 30 min to form a homogeneous mixture solution at environmental temperature. The pH of the solution was adjusted to 1 by using 1 M hydrochloric acid solution. Then the mixed solution was transferred into a 100 mL Teflon-lined stainless steel autoclave and heated at 160 °C for 12 h. Thereafter, the autoclave was cooled naturally to ambient temperature. The yellow precipitate was centrifuged and repeatedly washed with copious amounts of deionized water and ethanol. The final material, labeled as ZIS, was dried at 80 °C for 12 h.

The composites of BMO loaded with different weight percentages of ZIS (denoted as BMO + x%–

ZIS; $x = 2, 4, 6, 8, 10$) were synthesized by using a simple wet impregnation method. First of all, 0.3 g yellow BMO powders were dispersed in 50 mL methanol to form BMO suspension by ultrasonic method for 30 min. Then the calculated amount of ZIS was added into the suspension to stir at ambient temperature for 24 h in the fume hood. Afterward, the obtained solid materials were dried at 80 °C for 12 h.

Characterization

The structures and chemical properties of samples were studied by X-ray diffraction (XRD, Cu Kα, Purkinjie XD-3, 35 kV, 20 mA), FTIR (Nicolet-iS10), field-emission scanning electron microscopy (SEM, FEI Quanta 250F), transmission electron microscope (TEM, JEOL JEM-2100), X-ray photoelectron spectroscopy (XPS, PHI-5000C ESCA), nitrogen adsorption apparatus (Quantachrome, autosorb IQ), UV–vis diffuse reflection spectra (DRS, Shimadzu UV-2600, Photoluminescence spectra (PL, He-Cd laser, Labram-HR800). Ion chromatography (IC, DionexICS90) was employed to analyze ions in solution.

The test of photocatalytic activity

The photocatalytic activity test for NO removal was performed in a continuous flow reactor at environmental temperature and atmospheric pressure. The 200-mL cylindrical reactor consisted of stainless steel and covered with quartz glass. One Teflon omentum containing photocatalysts was placed in the middle of the reactor. A Xe lamp (350 W) was vertically placed above the reactor, which was used as visible light source.

Photocatalyst (0.1 g) was uniformly dispersed in a small piece of clean round cotton (d = 3.5 cm, h = 0.5 cm) and then placed on the Teflon omentum of the reactor. The premixed reactant gases (400 ppm NO, 7% O_2 and N_2 balance) were fed into the reactor at a total flow rate of 100 mL min^{-1}. After reaching adsorption–desorption equilibrium between gases and photocatalysts, 30% H_2O_2 solution was injected into the reactor via a peristaltic pump at a flow rate of 0.0075 mL min^{-1} to produce more active species for the PCO of NO and reduce the accumulation of reaction products on the surface of photocatalysts. Simultaneously, the Xe lamp was turned on and the experiment was started. The outlet concentration of NO was analyzed every 10 min by using SERVOMEX flue gas analyzer (Britain). The reaction of NO with O_2 was ignorable because there was little change of NO_2 concentration in the process of reaction product detection. Figure 1 depicts the schematic diagram of experimental apparatus. The removal efficiency of NO is defined as: NO conversion $\% = (NO_{in} - NO_{out})/NO_{in} \times 100\%$.

Detection of hydroxyl radicals

The hydroxyl radicals formed in the PCO of NO system were detected by using fluorescence technique, and terephthalic acid (TA) was used as a probe molecule. The detailed procedures were as follows: Four quartz tubes were labeled as the experimental groups (A–C) and control group (D), which were filled with 40 mL aqueous solution containing 0.3 mmol TA and 50 μL 30% H_2O_2 aqueous solution at environmental temperature. Then 10 mg BMO + 6%–ZIS composite photocatalyst was, respectively, dispersed in the solution of groups (A–C). Subsequently, all tubes were irradiated by Xe lamp (350 W) under stirring for 20 min (group A), 40 min (group B) and 60 min (groups C and D). After reaction, the ·OH concentration in the clear supernatant was measured by using FL3-TCSPC fluorescence spectrophotometer.

Trapping experiment of active species

As shown in Fig. S1, six quartz tubes were divided into four experimental groups (a–d) and two control groups (e–f). The groups (a–e) were filled with 40 mL deionized water and 4 mL 30% H_2O_2 solution, while the group (f) was only injected into 40 mL deionized water. Then 10 mg BMO + 6%–ZIS composite was added into group (a–d and f), respectively. Subsequently, 1 mL isopropyl alcohol (IPA) was injected into group (b) so that ·OH could be quenched, 0.1 mmol p-benzoquinone (BQ) was added into group (c) as the scavenger of $\cdot O_2^-$, 1 mL ethanol (EtOH) was put into group (d) in order that h^+ could be captured. Finally, NO was inputted in six quartz tubes, which were exposed to the visible light source under stirring condition for 30 min. After reaction, 1 mL of clear supernatant obtained was taken out and injected into IC to reveal effect of active species.

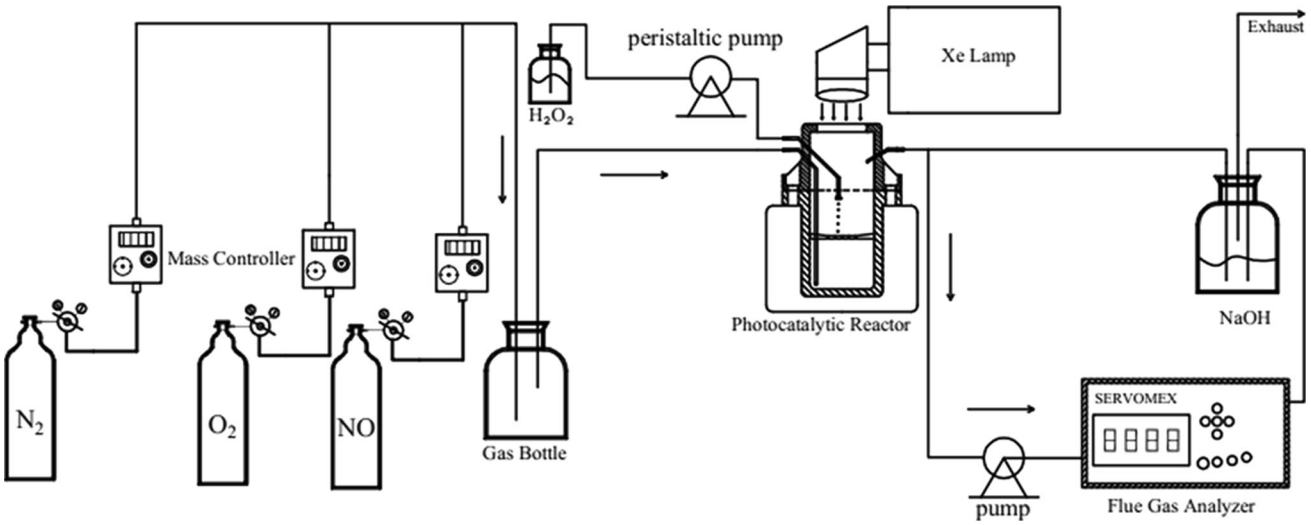

Figure 1 Schematic diagram of experimental apparatus for the PCO of NO.

Photoelectrochemical measurement

Photocurrent curves were conducted on the CHI 760B electrochemical workstation with a conventional three-electrode system using 0.5 mol L^{-1} Na_2SO_4 as electrolyte solution. The work electrode was prepared by the following process: 10 mg BMO + x%–ZIS powders were, respectively, dispersed in 1 mL ethanol containing 50 μL naphthol to form homogeneous suspension by ultrasonic method. The suspension was drop-coated on the exposed area of the conductive side of the FTO glass (1 cm × 0.5 cm) to form 1.6 mg cm^{-2} of the photocatalyst on the FTO, and then dried at 180 °C for 12 h in a vacuum oven.

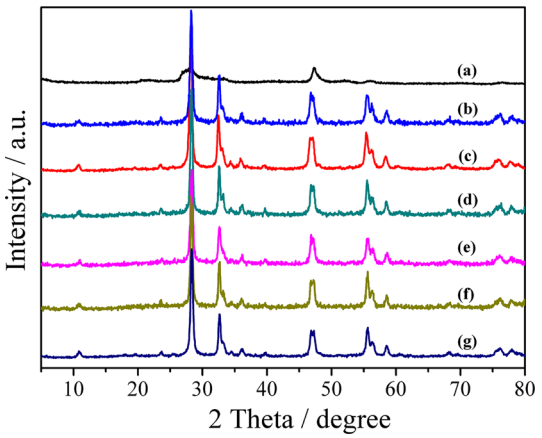

Figure 2 XRD of as-prepared samples: *a* ZIS, *b* BMO, *c* BMO + 2%–ZIS, *d* BMO + 4%-ZIS, *e* BMO + 6%–ZIS, *f* BMO + 8%–ZIS, *g* BMO + 10%–ZIS.

Result and discussion

Structural characterization

The crystal structures of as-prepared samples were identified by the patterns of XRD. As observed in Fig. 2 and Fig. S2, the pure ZIS sample shows the diffraction peaks at ca. 21.56°, 27.76°, 39.92 and 47.28°, which are, respectively, indexed as (006), (102), (108) and (110) crystal planes of the hexagonal ZIS (JCPDS No. 65-2023). For the pure BMO, the diffraction peaks at ca. 28.16°, 32.48°, 47.12° and 55.36° are indexed as (131), (002), (062) and (133) planes, respectively. The result indicates that the orthorhombic phase of BMO is in line with the JCPDS card No. 76-2388. No peaks indicating impurities were observed. In terms of the BMO + x%–ZIS (x = 2, 4, 6, 8, 10) composites, all the X-ray diffraction peaks of BMO are clearly observed, indicating the crystal structure of BMO cannot be influenced during the preparation process of BMO + x%–ZIS composite photocatalysts.

The FTIR spectra were also performed to investigate chemical structure of as-synthesized samples. As shown in Fig. 3, the absorption peaks at ca. 1396 and 1610 cm^{-1} corresponding to the hydroxyl group and surface absorbed water molecules are found for ZIS [31]. In terms of the pure BMO, the absorption bands at 500–950 cm^{-1} are related to Bi–O and Mo–O stretching and Mo–O–Mo bridging stretching modes. The absorption peaks at ca. 797 and 843 cm^{-1} are

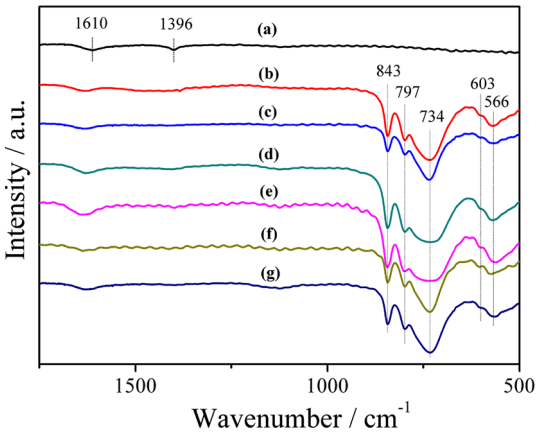

Figure 3 FTIR of as-prepared samples: *a* ZIS, *b* BMO, *c* BMO + 2%–ZIS, *d* BMO + 4%–ZIS, *e* BMO + 6%–ZIS, *f* BMO + 8%–ZIS, *g* BMO + 10%–ZIS.

labeled as the symmetric and asymmetric stretching modes of MoO_6 involving vibrations of apical oxygen atoms, respectively. The band at ca. 734 cm^{-1} is attributed to the asymmetric stretching mode of MoO_6 involving vibrations of the equatorial oxygen atoms. The peaks at 566 and 603 cm^{-1} correspond to the bending vibrations of MoO_6 [32]. More importantly, no obvious change is observed for the FTIR spectra of BMO + *x*%–ZIS ($x = 2$, 4, 6, 8, 10) composites in comparison with that of pure BMO. The result also indicates that the structure of BMO remains undamaged in the preparation process of BMO + *x*%–ZIS composites, which is consistent with the result of XRD.

To investigate the surface chemical composition of as-synthesized samples and the interaction between ZIS and BMO, the X-ray photoelectron spectroscopy (XPS) was performed. As shown in Fig. 4a, the survey spectra for BMO and ZIS indicate that C, Bi, Mo and O exist on the surface of BMO and C, Zn, In and S exist on the surface of ZIS and the survey spectrum for BMO + 6%–ZIS composite shows the existence of C, Bi, Mo, O, Zn, In and S on the surface of the composite photocatalyst. The C 1 s peak in the survey spectra results from the carbon tape used for fixing the sample or the adsorption of atmospheric CO_2 on the sample surface [21]. As for Fig. 4b–c, the peaks at 159.1 and 164.5 eV corresponding to the binding energy of Bi $4f_{7/2}$ and Bi $4f_{5/2}$ of BMO obviously shift toward high values. The peaks at 232.4 and 235.6 eV corresponding to the binding energies of Mo $3d_{5/2}$ and Mo $3d_{3/2}$ of BMO also show a slight shift to high values. The results demonstrate the existence of a strong interaction between BMO and ZIS. In the O 1 s spectra of Fig. 4d, the wide and asymmetric peak for BMO + 6%ZIS and BMO indicates the existence of more than one chemical state. The peaks at 529.9, 530.7, 531.9 eV for BMO + 6%ZIS, respectively, relate to Bi–O (lattice O), surface hydroxyl groups (O–H) and oxygen singly bonded to carbon (C–O) [19]. According to Fig. 4e–f, the peaks at 1021.8 and 1044.9 eV corresponding to Zn $2p_{3/2}$ and $2p_{1/2}$ of ZIS show a slight shift to low values, respectively, and the peaks at 444.9 and 452.5 eV corresponding to the binding energies of In $3d_{5/2}$ and $3d_{3/2}$ of ZIS also slightly shift to low values. The slight shifts of binding energy of Zn 2p and In 3d also indicate a effective electronic interaction between ZIS and BMO in the BMO + 6%ZIS composite.

The field-emission scanning electron microscopy (SEM) was employed to investigate the morphologies and macrostructures of as-synthesized samples intuitively. As depicted in Fig. 5a_1, a_2, the pure BMO is composed of flower-like microspheres. And the single spheres are assembled by nanoplates. For the SEM image of BMO + 6%–ZIS composite (Fig. 5b_1, b_2), we can find the BMO well attaches to the ZIS surface, thus contributing to the electron transfer between BMO and ZIS in the photocatalytic experimental process. As displayed in Fig. 5c_1, c_2, the pure ZIS is composed of a large number of microspheres with an average diameter of ca. 4 μm and presents a unique marigold-like spherical superstructure which is made up of copious nanosheets. This is supported by EDS mapping of Zn, In and S, which displays the homogeneous distribution of these elements (Fig. 5d–f). The energy-dispersive X-ray spectrum retrieved from the collected data of these maps (Fig. S3) demonstrates the presence of all relevant elements in the area. To further confirm effective construction of BMO + *x*%–ZIS composites, the HRTEM, EDX and corresponding mapping of BMO + 6%–ZIS composite have been performed. As shown in Fig. S4, it can be seen that the ZIS and BMO are connected together. The EDX indicates the existence of Bi, Mo, O, Zn, In and S in Z-scheme photocatalyst consisting of ZIS and BMO, which is in accordance with the XPS results. The elemental mapping images show a relative homogeneous distribution of Bi, Mo, O, C, Zn, In and S. The results are in accordance with that of SEM images. What's more, the specific surface areas of ZIS, BMO and BMO + 6%–ZIS composite are determined to be 179.27, 13.33 and 19.83 $m^2 \cdot g^{-1}$,

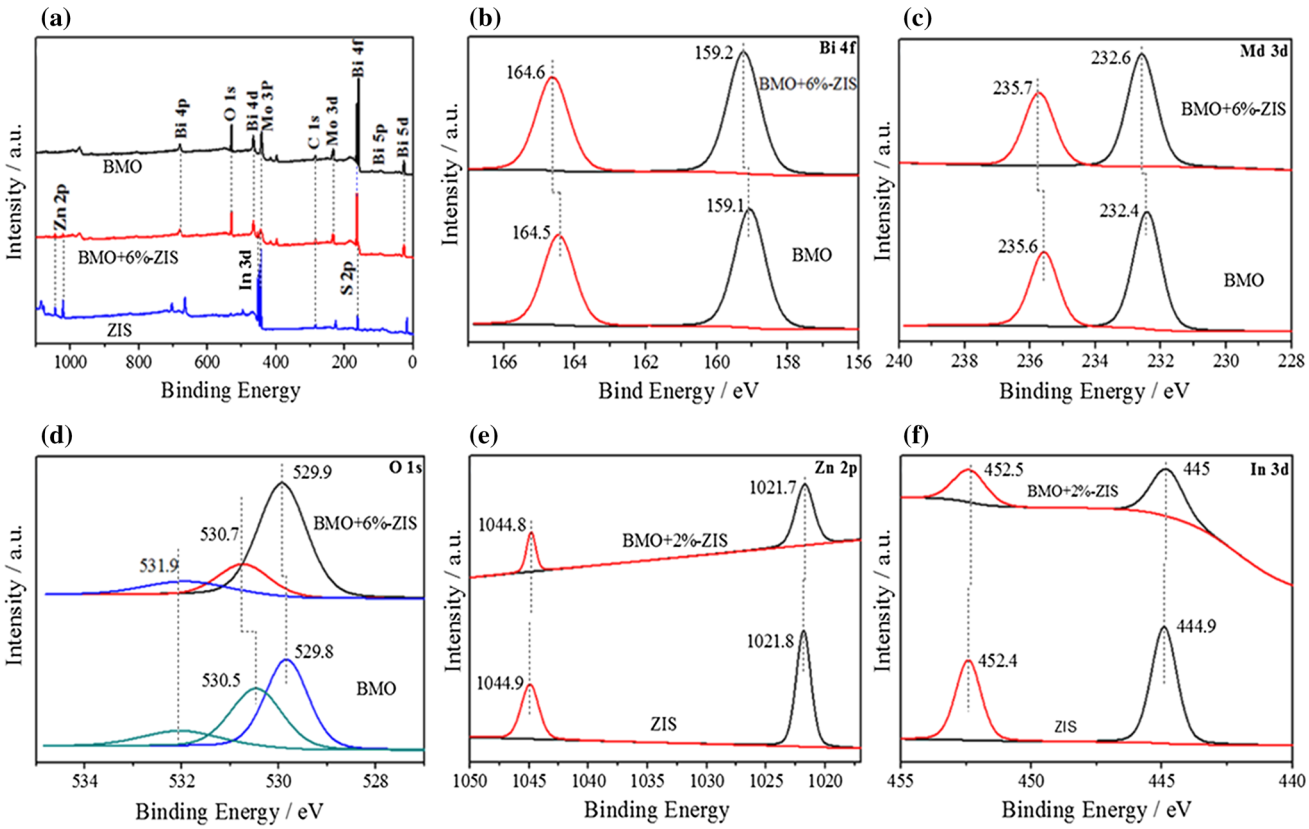

Figure 4 XPS survey spectra (**a**) and the high-resolution XPS spectra of Bi 4f (**b**), Mo 3d (**c**), O 1 s (**d**), Zn 2p(**e**), In 3d (**f**) regions for BMO, BMO +6%ZIS and ZIS.

respectively. The enhanced specific surface area of BMO + 6%–ZIS composite as compared to BMO can be ascribed to the introduction of ZIS with a high surface area, which can provide more restive sites to make the photocatalytic reaction more efficient.

To investigate the changes in the electronic properties of BMO + *x*%–ZIS composite, their photophysical properties were studied. UV–vis diffuse reflection spectra (DRS) of as-synthesized representative ZIS, BMO + 6%–ZIS composite and BMO are shown in Fig. 6. In the experiments, it can be found that the addition of ZIS is beneficial to the absorption of visible light, but only a minor redshift is observed. The phenomena imply that the intrinsic electronic properties of BMO do not change much. Also, the corresponding band gap (E_g) values for ZIS, BMO and BMO + 6%–ZIS are, respectively, calculated to be 1.98, 2.48 and 2.27 eV. According to previous reports, the valence band edge potentials (E_{VB}) and conduction band edge potentials (E_{CB}) of BMO are, respectively, estimated to be at −0.19 and + 2.29 eV [33], while the E_{CB} edge potentials of hexagonal phase ZIS are ca. −1.10 eV calculated by Mott-Schottky plots [26] and the corresponding E_{VB} edge potential is ca. + 0.88 eV.

Enhanced photocatalytic activity of NO oxidation

The as-prepared BMO + *x*%–ZIS (*x* = 0, 2, 4, 6, 8, 10) composite photocatalysts were applied in the experiment of PCO of NO under visible light so that their performances of air purification could be evaluated. In advance, four control experiments were performed in the absence of BMO + 6%–ZIS, the visible light, H_2O_2 solution, both BMO + 6%–ZIS and H_2O_2 solution. As shown in Fig. S5, the corresponding NO removal rates are low, indicating that it is difficult for NO to be fully oxidized or photolyzed under corresponding experimental conditions. Thereafter, the visible-light-induced PCO performances of BMO + *x*%–ZIS composites on NO oxidation were performed. The gas streams were introduced into the

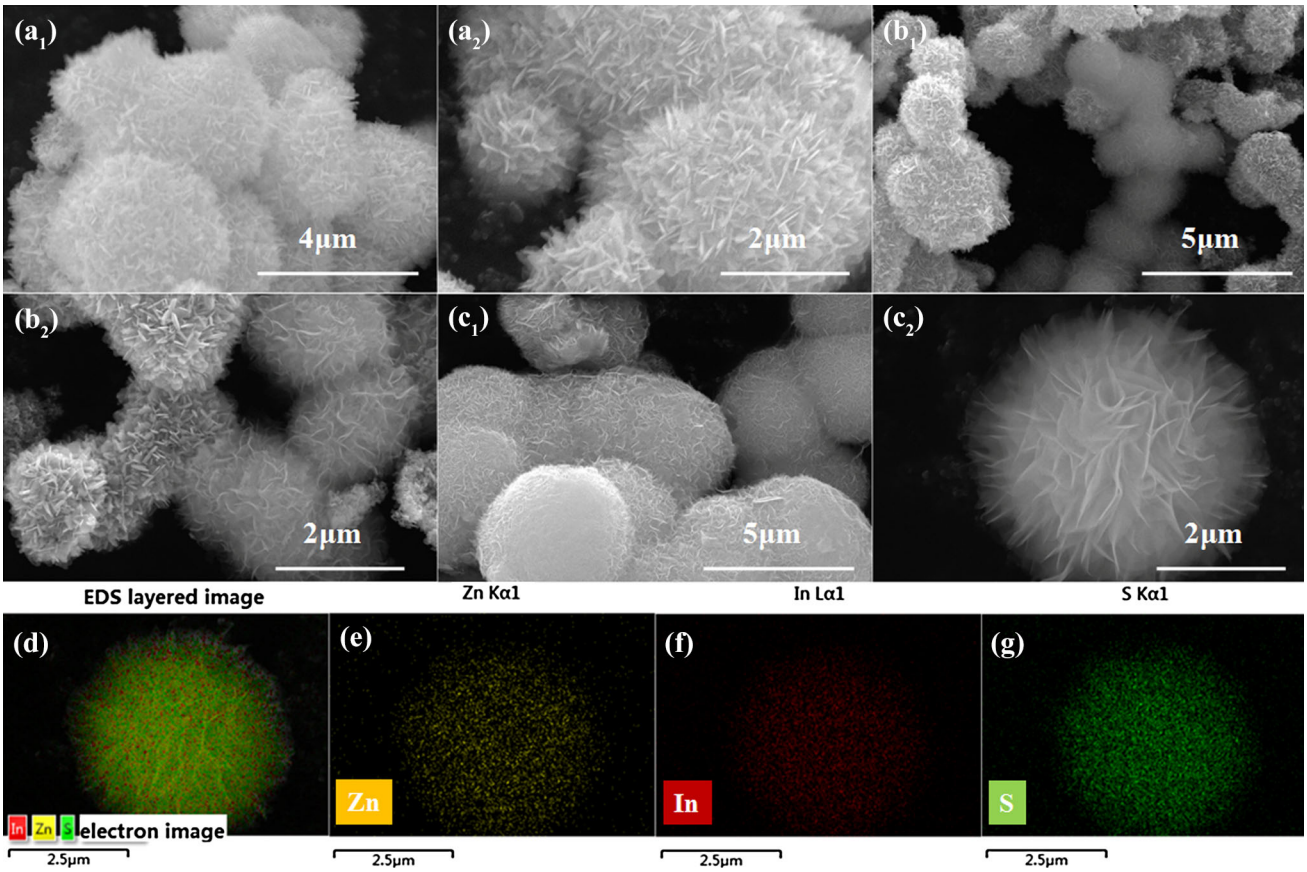

Figure 5 SEM of as-prepared samples: BMO ($\mathbf{a_1}$ and $\mathbf{a_2}$), BMO + 6%–ZIS ($\mathbf{b_1}$ and $\mathbf{b_2}$) and ZIS ($\mathbf{c_1}$ and $\mathbf{c_2}$) along with EDS layered image (**d**), Zn (**e**), In (**f**) and S (**g**) EDS mapping.

photocatalytic reactor after being premixed completely. When the adsorption–desorption equilibrium between gases and photocatalysts was reached, the Xe lamp and the peristaltic pump delivering H_2O_2 solution were turned on and the experiment was started. As shown in Fig. 7a, it can be seen that the efficiency of PCO of NO gradually increases with the light irradiation time and then reaches chemical equilibrium. The photocatalytic activity for BMO + x%–ZIS (x = 2, 4, 6, 8, 10) composites exhibits much enhancement compared with the pure BMO, which is also higher than that of control experiment with the absence of BMO + 6%–ZIS or light. In particular, it is worth noting that BMO + 6%–ZIS composite evidently exhibits the highest photocatalytic activity on NO removal, reaching 84.94% in 80 min. As compared to our previous reports in Table S1, it can be found the effectively constructed Z-scheme BMO + x%–ZIS composites possess much higher photocatalytic performances due to the efficient separation of photoinduced electrons and holes. The stability of a catalyst is also an important parameter from the point of practical applications. Therefore, the stability tests for the PCO of NO over BMO + 6%–ZIS photocatalyst have been carried out. As shown in Fig. 7b, the BMO + 6%–ZIS composite can maintain a good photocatalytic activity and recyclability in the process of PCO of NO. The photocatalytic efficiency with a slight decrease after three cycles can be attributed to the increased accumulation amount of generated oxidation products on the surface of photocatalysts, which covered restive sites and impeded the formation of the active species. What's more, the stability of BMO + 6%–ZIS before and after photocatalytic reaction was also investigated by FTIR spectra (Fig. 8). There is no obvious change and merely a new peak of NO_3^- at ca. 1384 cm^{-1} without the peak of NO_2^-. Thus, the BMO + x%–ZIS composite photocatalyst is stable and efficient. The results also indicate that NO_3^- is the primary product in the process of PCO of NO.

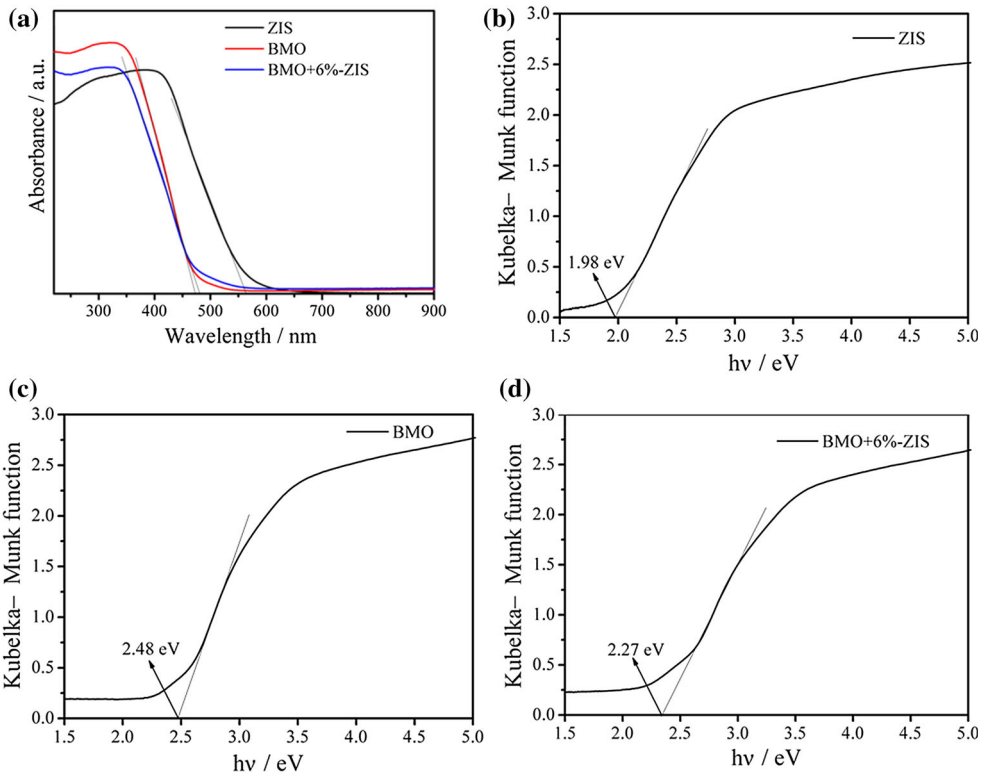

Figure 6 **a** UV–vis diffuse reflection spectra and **c**–**d** corresponding derived plots of transformed Kubelka–Munk function of as-prepared representative ZIS, BMO + 6%–ZIS and BMO.

Ion chromatography (IC) was employed to detect the composition of PCO of NO reaction products. After one experiment was finished completely, the photocatalyst and the small piece of cotton which ion adhered to were transferred to a quartz tube. Then the quartz tube was placed overnight in order that ions on the surface of the photocatalyst after reaction could dissolve into the solution completely. 8 mL deionized water was added into the mixture in advance. Thereafter, 1 mL of the clear supernatant obtained by centrifugation was diluted 50 times with deionized water and injected into IC at last. The qualitative analytical result, taking BMO + 6%–ZIS composite for an instance, is shown in Fig. S6, which indicates the existence of NO_3^- in the solution. Additionally, there was no increase in NO_2 during the experimental process. And NO_2^- was not detected in the IC. These results could be ascribed to the introduction of H_2O_2, which had produced considerable amount of active species in the presence of BMO + 6%–ZIS composite and made the oxidative ability of the system enhanced. Therefore, NO_3^- can be regarded as the photocatalytic oxidation reaction product. The standard solution was prepared, and their corresponding IC was conducted. And the fitting line is shown in Fig. S7. Consequently, the concentration value of NO_3^- in the solution could be obtained through external standard method. Also, nitrogen balance calculation was performed to investigate the possible byproducts, and the corresponding calculated process is given in the support information. The results further demonstrate not only that NO_3^- is the reaction product in the experiment of PCO of NO, but also well corresponds with that of visible-light-driven PCO performance of BMO + 6%–ZIS composite on NO removal, which indicates the accuracy and reliability of the PCO experimental results.

The photoluminescence (PL) technique is regarded as a useful method to reveal the transfer and separation efficiency of photoinduced electrons and holes in the semiconductor particles [34]. Ordinarily, a lower PL intensity indicates a lower recombination of photoinduced charge carriers, thus obtaining an enhanced photocatalytic activity [35]. Herein, the PL spectra were employed to study changes in the electronic properties of the as-synthesized representative ZIS, BMO + 6%–ZIS and BMO. As observed in Fig. 9a, the pure ZIS presents a high PL intensity at 325 nm excitation. Compared with the pure ZIS, the BMO + 6%–ZIS composite displays a lower PL intensity, but possesses a higher PL intensity than

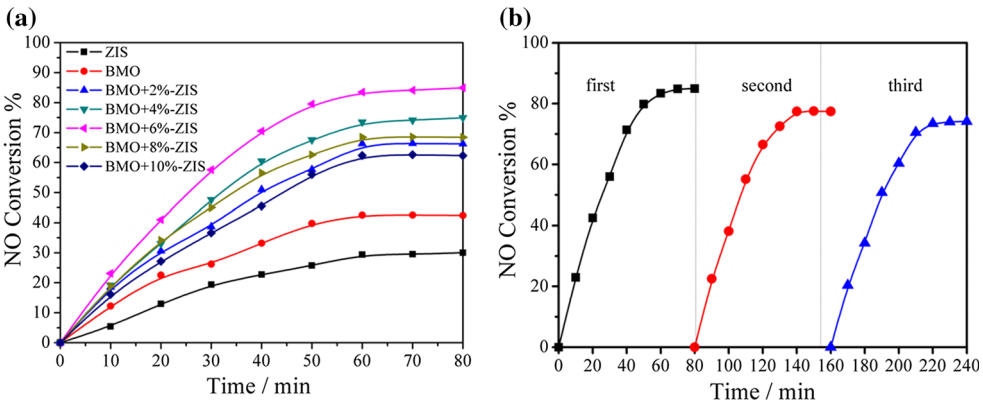

Figure 7 **a** The NO conversion efficiency of as-prepared samples: ZIS, BMO, BMO + 2%–ZIS, BMO + 4%–ZIS, BMO + 6%–ZIS, BMO + 8%–ZIS and BMO + 10%–ZIS; **b** the stability tests of BMO + 6%–ZIS composite for NO removal under visible light.

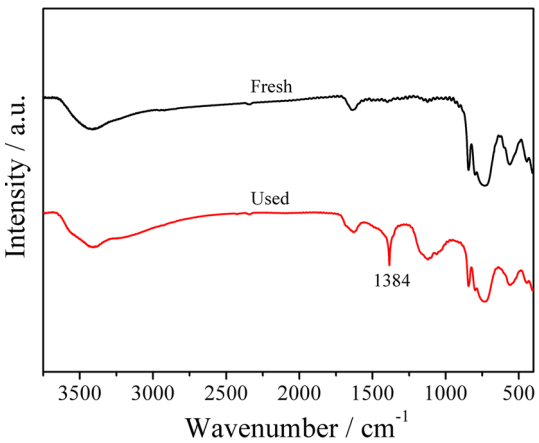

Figure 8 FTIR spectra of BMO + 6%–ZIS before and after the PCO of NO reaction.

pure BMO. The result is opposite to that of general PL experiments. Through reviewing the experimental procedures and studying relative literature [36], it might be implied that the photoinduced electrons and holes in the BMO + 6%–ZIS composite are not transferred as shown in Fig. 11a but as in Fig. 11b. The higher PL intensity of BMO + 6%–ZIS originates from the higher recombination rate between photoinduced electrons in the CB of BMO and holes in the VB of ZIS, thus leaving rich electrons in the CB of ZIS and holes in the VB of BMO to participate in photocatalytic reaction. The analytical result demonstrates that the construction of BMO + x%–ZIS composite photocatalysts contributes to the separation of photoinduced charge carriers. In addition, to further validate the improvement of photogenerated electron–hole migration and separation, the photocurrent of the BMO + 6%–ZIS composite was also investigated during on and off cycles of irradiation. As depicted in Fig. 9b, the ZIS exhibits a higher photocurrent density than BMO, while the BMO + 6%–ZIS composite possesses much higher photocurrent density in comparison with pure ZIS. The above results not only demonstrate that the introduction of BMO could promote efficient separation of photoinduced electrons and holes to enhance the photocatalytic activity of BMO + 6%–ZIS composite, but also imply that the constructed BMO + 6%–ZIS composite photocatalyst is available in the PCO of NO system.

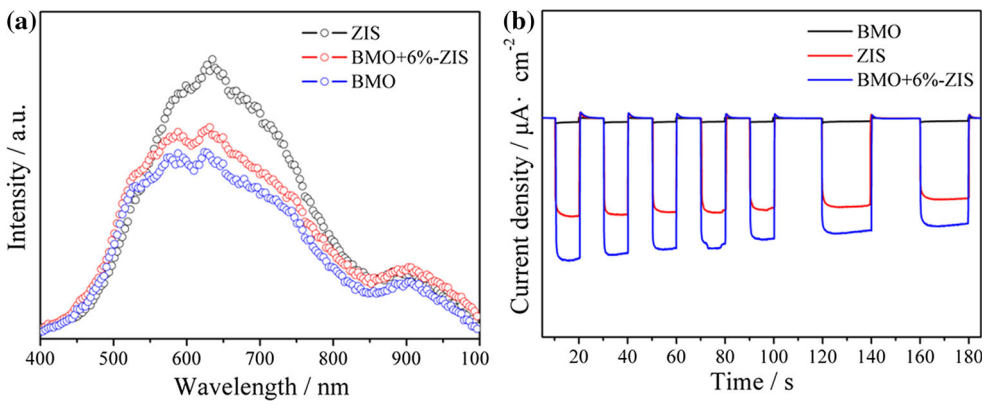

Figure 9 Photoluminescence spectra (**a**) and photocurrent density curves (**b**) of as-synthesized representative ZIS, BMO + 6%–ZIS and BMO.

Mechanism analysis of photocatalytic activity

PL spectra and photocurrent curves confirm effective separation of photoinduced electrons and holes in the constructed BMO + 6%–ZIS composite photocatalyst. As is known to all, the photocatalytic efficiency of a reaction system relies not only on the separation rate of the photoinduced electrons and holes, but also on the production and participation of active radical species. What's more, the quantitative analysis results of IC have indicated that NO_3^- is the photocatalytic reaction product in the PCO of NO system. It is inferred that more active substances could react with electrons and holes to produce active species. To further ascertain the enhancement in photocatalytic activity for BMO + *x*%–ZIS composite photocatalysts, we determined the contribution of active radical species in the photocatalytic reaction using trapping experiments and fluorescence spectra.

Initially, the fluorescence spectra using terephthalic acid (TA) as probe molecule were conducted to detect ·OH [37]. The fluorescence spectra of control group and experimental groups with BMO + 6%–ZIS composite were performed with an excitation wavelength of 315 nm. As shown in Fig. 10, the fluorescence emission peak occurred at ca. 426 nm, indicating that 2-hydroxy terephthalic acid was formed from the reaction between ·OH and TA under visible light irradiation. Furthermore, the fluorescence intensity of experimental groups (A–C) is much higher than that of the control group and gradually increases with time. The results indicate that large amounts of ·OH is generated in the presence of BMO + 6%–ZIS in the process of PCO of NO. To further explore the role of other active species introduced in the PCO of NO system, the trapping experiment, taking BMO + 6%–ZIS composite for an instance, was carried out to investigate the involvement of active radical species. The qualitative analytical result displays that the NO_3^- concentrations of the experimental groups (a–d) and control groups (e–f) are 15.82, 4.57, 5.34, 10.27, 3.27 and 9.62 mg·L^{-1}, respectively. The NO_3^- concentration value of group (b) unaffected by ·OH is lower than any other experimental group and only a little higher than that of control group (e), which indicates that ·OH plays an important role in the PCO of NO. Additionally, the NO_3^- concentration value of group (c) excluding the impact of $\cdot O_2^-$ is only little higher than that of group (b), and still in a low level

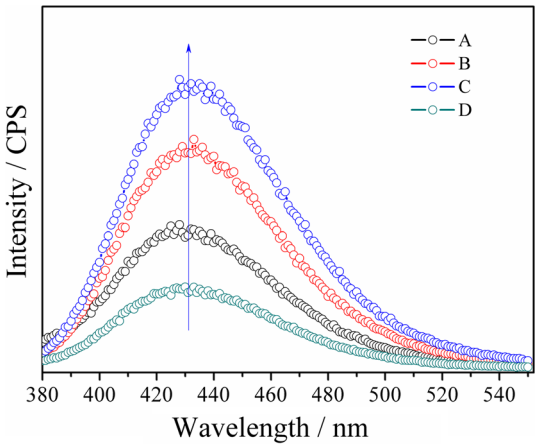

Figure 10 Fluorescence spectra of TAOH solutions generated by the experimental group with BMO + 6%–ZIS for 20 min (*A*), 40 min (*B*), 60 min (*C*) and the control group for 60 min (*D*) under visible light.

in comparison with that of group (a). The results imply that $\cdot O_2^-$ does not play a decisive effect, but is also essential and efficiency in the PCO of NO. It is worth mentioning that the result of group (d) implies that h^+ has weak oxidation ability and could directly oxidize NO to a certain extent in the PCO of NO system. From what has been discussed above, it can be concluded that the order to contributing to the PCO of NO is ·OH > $\cdot O_2^-$ > h^+ in the PCO of NO experimental system and the ·OH plays an important role but the effect of $\cdot O_2^-$ is also crucial. Meanwhile, we can find the NO_3^- concentration of group (f) is lower than that of group (a). The result indicates that the injected H_2O_2 solution can produce more active species to promote the photocatalytic activity due to the reaction between photoinduced charge carriers and H_2O_2.

Based on the foregoing results and the band gap structure of BMO and ZIS, the possible mechanism for enhanced photocatalytic activity of BMO + 6%–ZIS composite was proposed as shown in Fig. 11. Once irradiating with visible light, electrons can be photoexcited from valence band of ZIS and BMO to their corresponding conduction bands. If the coupling of ZIS and BMO forms a heterojunction-type composite photocatalyst, the photoinduced electrons and holes transfer process occur as displayed in Fig. 11a, which is the most common photogenerated charges and holes separation process for large amounts of composite photocatalysts. The photoinduced electrons are separated by the migration of the electrons from the CB of the ZIS to the CB of the

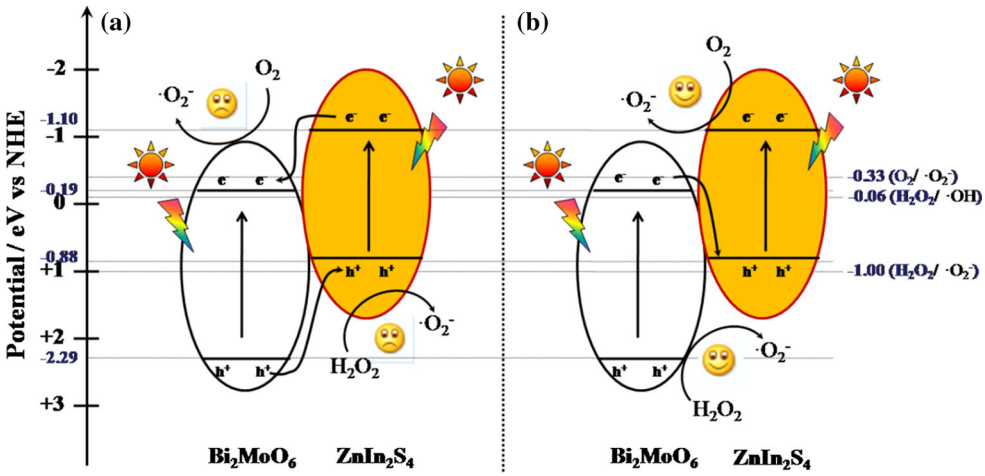

Figure 11 Schematic representation of **a** heterojunction-type electron–hole transfer mechanisms **b** Z-scheme electron–hole transfer mechanisms.

BMO, while the holes in the VB of BMO simultaneously migrate into the VB of ZIS. This can offer the efficient separation of the photogenerated electrons and holes. But the accumulated holes on the VB of ZIS cannot oxidize water molecules and hydrogen peroxide molecules to produce $\cdot O_2^-$ radicals. Similarly, the electron on the CB of BMO cannot reduce oxygen molecules (O_2) into $\cdot O_2^-$. Because the CB potential of BMO (−0.19 eV) is more positive than the redox potential of $\cdot O_2^-$ formation ($O_2/\cdot O_2^-$ = −0.33 eV) [38] and the VB potential of the ZIS (+0.88 eV) is more negative than the potential required to oxidize H_2O_2 to $\cdot O_2^-$ (+1.00 eV) [39]. Therefore, if the charge carriers transfer follows as shown in Fig. 11a, then the composite photocatalyst only forms the production of ·OH ($H_2O_2/\cdot OH$ = + 0.06 eV) [39], but not has the production of the $\cdot O_2^-$ in the PCO of NO. The obtained results contradict that of trap experiments which demonstrate that $\cdot O_2^-$ is also a crucial active species in the reaction and increase the photocatalytic activity of BMO + *x*%–ZIS composites. In contrast, if the coupling of ZIS and BMO follows the Z-scheme mechanism as depicted in Fig. 11b. It is not only consistent with the result of fluorescence spectra, but also well corresponds with the trapping experimental results that the concentration of NO_3^- is obviously decreased after the addition of IPA and BQ scavengers. The photoinduced electrons in the CB of BMO are transferred to the VB of the ZIS, where they recombine with holes in the VB of the ZIS. Hence, the electrons in the CB of the ZIS and the holes in the VB of the BMO are well separated, which effectively participate in the reaction with H_2O_2 molecule to produce large amounts of active free radicals and enhance the photocatalytic activity of BMO + 6%–ZIS composite. Because the higher positive VB potential of BMO (+2.29 eV) can easily oxidize H_2O_2 to $\cdot O_2^-$ ($H_2O_2/\cdot O_2^-$ = + 1.00 eV). Similarly, the higher negative CB potential of ZIS (−1.10 eV) can availably reduce O_2 to $\cdot O_2^-$ ($O_2/\cdot O_2^-$ = −0.33 eV). The large amounts of active free radicals ($\cdot O_2^-$, ·OH) would form a strong oxidation ability in the BMO + *x*%–ZIS composite photocatalysts, thus leading to an enhanced photocatalytic performance compared with the individual ZIS or BMO photocatalyst. As a matter of fact, many similar direct Z-scheme photocatalytic systems (e.g., $CaIn_2S_4/TiO_2$ [23], g-C_3N_4/Ag_3PO_4 [40], g-C_3N_4/TiO_2 [41]) have been reported and all of them exhibit efficient separation and transfer of photoinduced electrons and holes, thus resulting in a high-efficiency photocatalytic activity.

Conclusions

In this work, Z-scheme BMO + *x*%–ZIS (*x* = 2, 4, 6, 8, 10) composite photocatalysts were successfully synthesized by a facial wet impregnation method. The BMO + *x*%–ZIS composites exhibit enhanced photocatalytic activity compared with that of pure BMO. More importantly, BMO + 6%–ZIS composite displays the highest photocatalytic efficiency in the experiment of PCO of NO. The trapping experiments, hydroxyl radical detection results and photocurrent analysis proved that the enhanced photocatalytic performance of BMO + 6%–ZIS could be ascribed to

the Z-scheme migration of the photogenerated electrons and holes. The reaction production is NO_3^- as confirmed by ion chromatography and FTIR spectra. In addition, the mechanism of PCO of NO indicates that the order to contributing to the PCO of NO is $\cdot OH > \cdot O_2^- > h^+$ and the ·OH plays an important role but the effect of $\cdot O_2^-$ is also crucial in the PCO of NO system.

Acknowledgements

This work was financially supported by the Key Project of Chinese National Programs for Research and Development (2016YFC0203800). Assembly Foundation of the Industry and Information Ministry of the People's Republic of China 2012 (543), the National Natural Science Foundation of China (51408309 and 51578288), Science and Technology Support Program of Jiangsu Province (BE2014713), Natural Science Foundation of Jiangsu Province (BK20140777), Industry-Academia Cooperation Innovation Fund Projects of Jiangsu Province (BY2014004-10), Science and technology project of Nanjing (201306012), Jiangsu Province Scientific and Technological Achievements into a Special Fund Project (BA2015062), Top-notch Academic Programs of Jiangsu Higher Education Institutions, A Project by the Priority Academic Program Development of Jiangsu Higher Education Institutions.

Electronic supplementary material: The online version of this article (doi:10.1007/s10853-017-1283-3) contains supplementary material, which is available to authorized users.

References

[1] Liu XL, Li D, Yang WT, Tang SL, Li XH, Fan LZ, Li YC (2016) Controlled calcination of ZnSe and ZnTe nanospheres to prepare visible-light catalysts with enhanced photostability and photoactivity. J Mater Sci 51:11021–11037

[2] Wang MJ, Shen SL, Li L, Tang ZH, Yang JH (2017) Effects of sacrificial reagents on photocatalytic hydrogen evolution over different photocatalysts. J Mater Sci 52:5155–5164

[3] Wan SP, Zhong Q, Ou M, Zhang SL (2016) Highly efficient simulated solar-light photocatalytic oxidation of gaseous NO with porous carbon nitride from copolymerization with thymine and mechanism analysis. RSC Adv 6:101208–101215

[4] Ho WK, Zhang ZZ, Lin W, Huang SP, Zhang XW, Wang XW, Huang Y (2016) Copolymerization with 2,4,6-triaminopyrimidine for the rolling-up the layer structure, tunable electronic properties, and photocatalysis of g-C_3N_4. Appl Mater Interfaces 7:5497–5505

[5] McFarland EW, Metiu H (2013) Catalysis by doped oxides. Chem Rev 113:4391–4427

[6] Fujishima A, Honda K (1972) Electrochemical photolysis of water at a semiconductor electrode. Nature 238:37–38

[7] Jin M, Lu SY, Ma L, Gan MY (2017) One-step synthesis of in situ reduced metal Bi decorated bismuth molybdate hollow microspheres with enhancing photocatalytic activity. Appl Surf Sci 396:438–443

[8] Wang WR, An YT, Chen LF, Qi ZW (2017) Visible-light-driven Ag_2MoO_4/Ag_3PO_4 composites with enhanced photocatalytic activity. J Alloys Compd 701:350–357

[9] Huang ZF, Song JJ, Li K et al (2016) Hollow cobalt-based bimetallic sulfide polyhedra for efficient all-pH-value electrochemical and photocatalytic hydrogen evolution. J Am Chem Soc 138:1359–1365

[10] Manzi A, Simon T, Sonnleitner C et al (2015) Light-induced cation exchange for copper sulfide based CO_2 reduction at ambient pressure. J Am Chem Soc 137:14007–14010

[11] Tian GH, Chen YJ, Zhou W, Pan K, Dong YZ, Tian CG, Fu HG (2011) Facile solvothermal synthesis of hierarchical flower-like Bi_2MoO_6 hollow spheres as high performance visible-light driven photocatalysts. J Mater Chem 21:887–892

[12] Ou M, Zhong Q, Zhang SL, Nie HY, Lv ZJ, Cai W (2016) Graphene-decorated 3D $BiVO_4$ superstructure: highly reactive (040) facets formation and enhanced visible-light-induced photocatalytic oxidation of NO in gas phase. Appl Catal B 193:160–169

[13] Huang HW, Wang JJ, Dong F, Guo YX, Tian N, Zhang YH, Zhang TR (2015) Highly efficient $Bi_2O_2CO_3$ single-crystal lamellas with dominantly exposed 001 facets. Cryst Growth Des 15:534–537

[14] Huang YK, Kang SF, Yang Y, Qin HF, Ni ZJ, Yang SJ, Li X (2016) Facial synthesis of Bi/Bi_2WO_6 nanocomposite with enhanced photocatalytic activity under visible light. Appl Catal B 196:89–99

[15] Gnayem H, Sasson Y (2013) Hierarchical nanostructured 3D flowerlike BiOClxBr 1–x semiconductors with exceptional visible light photocatalytic activity. ACS Catal 3:186–191

[16] Peng Y, Wang KK, Liu T, Xu J, Xu BG (2017) Synthesis of one-dimensional Bi_2O_3–$Bi_2O_{2.33}$ heterojunctions with high interface quality for enhanced visible light photocatalysis in degradation of high-concentration phenol and MO dyes. Appl Catal B 203:946–954

[17] Han PL, Mihi A, Ferre-borrull J, Pallarés J, Marsal LF (2015) Interplay between morphology, optical properties, and electronic structure of solution-processed Bi_2S_3 colloidal nanocrystals. J Phys Chem C 119:10693–10699

[18] Shimodaira Y, Kato H, Kobayashi H, Kudo A (2006) Photophysical properties and photocatalytic activities of bismuth molybdates under visible light irradiation. J Phys Chem B 110:17790–17797

[19] Xu YS, Zhang WD (2013) Anion exchange strategy for construction of sesame-biscuit-like $Bi_2O_2CO_3$/Bi2MoO_6 nanocomposites with enhanced photocatalytic activity. Appl Catal B 140–141:306–316

[20] Zou JP, Luo SL, Zhang LZ et al (2013) One-pot solvothermal syntheses of ternary heterostructured TiO_2–Bi_2MoO_6/$Bi_{3.64}Mo_{0.36}O_{6.55}$ controllable in terms of composition, morphology and structure: materials of high visible-light driven photocatalytic activity. Appl Catal B 140–141:608–618

[21] Zhang MY, Shao CL, Mu JB et al (2012) Hierarchical heterostructures of Bi_2MoO_6 on carbon nanofibers: controllable solvothermal fabrication and enhanced visible photocatalytic properties. J Mater Chem 22:577–584

[22] Gou XL, Cheng FY, Shi YH, Zhang L, Peng SJ, Chen J, Shen PW (2006) Shape-controlled synthesis of ternary chalcogenide $ZnIn_2S_4$ and CuIn(S, Se)$_2$ nano-/microstructures via facile solution route. J Am Chem Soc 128:7222–7229

[23] Jo WK, Natarajan TS (2015) Facial synthesis of novel redox-mediator-free direct Z-scheme $CaIn_2S_4$ marigold-flower-like/TiO_2 photocatalysts with superior photocatalytic efficiency. ACS Appl Mater Interfaces 7:17138–17154

[24] Chen X, Li L, Zhang WZ, Li YX, Song Q, Dong L (2016) Fabricate globular flower-like CuS/$CdIn_2S_4$/$ZnIn_2S_4$ with high visible light response via microwave-assisted one-step method and its multipathway photoelectron migration properties for hydrogen evolution and pollutant degradation. ACS Sustain Chem Eng 4:6680–6688

[25] Chen YJ, Hu SW, Liu WJ et al (2011) Controlled syntheses of cubic and hexagonal $ZnIn_2S_4$ nanostructures with different visible-light photocatalytic performance. Dalton Trans 40:2607–2613

[26] Chen YJ, Huang RK, Chen DQ, Wang YS, Liu WJ, Li XN, Li ZH (2012) Exploring the different photocatalytic performance for dye degradations over hexagonal $ZnIn_2S_4$ microspheres and cubic $ZnIn_2S_4$ nanoparticles. ACS Appl Mater Interfaces 4:2273–2279

[27] Shang L, Zhou C, Bian T, Yu HJ, Wu LZ, Tung CH, Zhang TR (2013) Facile synthesis of hierarchical $ZnIn_2S_4$ submicrospheres composed of ultrathin mesoporous nanosheets as a highly efficient visible-light-driven photocatalyst for H_2 production. J Mater Chem A 1:4552–4558

[28] Tian F, Zhu RS, Song KL, Ouyang F, Cao G (2015) The effects of amount of La on the photocatalytic performance of $ZnIn_2S_4$ for hydrogen generation under visible light. Int J Hydrog Energy 40:2141–2148

[29] Gao B, Dong SN, Liu JD et al (2016) Identification of intermediates and transformation pathways derived from photocatalytic degradation of five antibiotics on $ZnIn_2S_4$. Chem Eng J 304:826–840

[30] Chen JS, Xin F, Yin XH, Xiang TY, Wang YW (2015) Synthesis of hexagonal and cubic ZnIn2S4 nanosheets for the photocatalytic reduction of CO_2 with methanol. RSC Adv 5:3833–3839

[31] Li HF, Yu HT, Chen S, Zhao HM, Zhang YB, Quan X (2014) Fabrication of graphene wrapped $ZnIn_2S_4$ microspheres heterojunction with enhanced interfacial contact and its improved photocatalytic performance. Dalton Trans 43:2888–2894

[32] Zhang LW, Xu TG, Zhao X, Zhu YF (2010) Controllable synthesis of Bi_2MoO_6 and effect of morphology and variation in local structure on photocatalytic activities. Appl Catal B 98:138–146

[33] Li HP, Liu JY, Hou WG, Du N, Zhang RJ, Tao XT (2014) Synthesis and characterization of g-C_3N_4/Bi_2MoO_6 heterojunctions with enhanced visible light photocatalytic activity. Appl Catal B 160–161:89–97

[34] Martha S, Nashim A, Parida KM (2013) Facile synthesis of highly active g-C_3N_4 for efficient hydrogen production under visible light. J Mater Chem A 1:7816–7824

[35] Jiang DL, Chen LL, Zhu JJ, Chen M, Shi WD, Xie JM (2013) Novel p–n heterojunction photocatalyst constructed by porous graphite-like C_3N_4 and nanostructured BiOI: facile synthesis and enhanced photocatalytic activity. Dalton Trans 42:15726–15734

[36] Chen S, Ji L, Tang W, Fu X (2013) Fabrication, characterization and mechanism of a novel Z-scheme photocatalyst $NaNbO_3$/WO_3 with enhanced photocatalytic activity. Dalton Trans 42:10759–10768

[37] Hirakawa T, Nosaka Y (2002) Properties of $O_2{\cdot}^-$ and OH· formed in TiO_2 aqueous suspensions by photocatalytic reaction and the influence of H_2O_2 and some ions. Langmuir 18:3247–3254

[38] Dong F, Zhao ZW, Sun YJ, Zhang YX, Yan S, Wu ZB (2015) An advanced semimetal-organic Bi spheres–g-C_3N_4 nanohybrid with SPR-enhanced visible-light photocatalytic performance for NO purification. Environ Sci Technol 49:12432–12440

[39] Nie H, Ou M, Zhong Q, Zhang SL, Yu LM (2015) Efficient visible-light photocatalytic oxidation of gaseous NO with graphitic carbon nitride (g-C_3N_4) activated by the alkaline

hydrothermal treatment and mechanism analysis. J Hazard Mater 300:598–606

[40] Chen XX, Huang XT, Yi ZG (2014) Enhanced ethylene photodegradation performance of g-C_3N_4–Ag_3PO_4 composites with direct Z-scheme configuration. Chem Eur J 20:17590–17596

[41] Yu JG, Wang SH, Low JX, Xiao W (2013) Enhanced photocatalytic performance of direct Z-scheme g-C_3N_4–TiO_2 photocatalysts for the decomposition of formaldehyde in air. Phys Chem Chem Phys 15:16883–16890